
















NGTS-19b: a high-mass transiting brown dwarf in a 17-d eccentric orbit

Jack S. Acton ^{1,★}, Michael R. Goad,¹ Matthew R. Burleigh,¹ Sarah L. Casewell,¹ Hannes Breytenbach,^{2,3} Louise D. Nielsen ⁴, Gareth Smith,⁵ David R. Anderson ^{6,7}, Matthew P. Battley ^{6,7}, Daniel Bayliss ^{6,7}, François Bouchy,⁴ Edward M. Bryant,^{6,7} Szilárd Csizmadia ⁸, Philipp Eigmüller,⁸ Samuel Gill,^{6,7} Edward Gillen ^{9,5†}, Nolan Grieves,⁴ Maximilian N. Günther ^{10‡}, Beth A. Henderson,¹ Simon T. Hodgkin,¹¹ James A. G. Jackman ^{6,7,12}, James S. Jenkins ^{13,14}, Monika Lendl ⁴, James McCormac,^{6,7} Maximiliano Moyano,¹⁵ Richard P. Nelson,⁹ Ramotholo R. Sefako,² Alexis M. S. Smith,⁸ Manu Stalport,⁴ Jessymol K. Thomas,² Rosanna H. Tilbrook,¹ Stéphane Udry,⁴ Richard G. West ^{6,7}, Peter J. Wheatley ^{6,7}, Hannah L. Wouters,² Jose I. Vines ¹³ and Douglas R. Alves ¹³

¹School of Physics and Astronomy, University of Leicester, University Road, Leicester LE1 7RH, UK

²South African Astronomical Observatory, PO Box 9, Observatory 7935, Cape Town, South Africa

³Department of Astronomy, University of Cape Town, Rondebosch 7700, Cape Town, South Africa

⁴Observatoire de Genève, Université de Genève, 51 Ch. des Maillettes, CH-1290 Sauverny, Switzerland

⁵Astrophysics Group, Cavendish Laboratory, J.J. Thomson Avenue, Cambridge CB3 0HE, UK

⁶Centre for Exoplanets and Habitability, University of Warwick, Gibbet Hill Road, Coventry CV4 7AL, UK

⁷Department of Physics, University of Warwick, Gibbet Hill Road, Coventry CV4 7AL, UK

⁸Institute of Planetary Research, German Aerospace Center, Rutherfordstrasse 2, D-12489 Berlin, Germany

⁹Astronomy Unit, Queen Mary University of London, Mile End Road, London E1 4NS, UK

¹⁰Department of Physics, Kavli Institute for Astrophysics and Space Research, Massachusetts Institute of Technology, Cambridge, MA 02139, USA

¹¹Institute of Astronomy, University of Cambridge, Madingley Road, Cambridge CB3 0HA, UK

¹²School of Earth and Space Exploration, Arizona State University, Tempe, AZ 85287, USA

¹³Departamento de Astronomía, Universidad de Chile, Casilla 36-D, Santiago, Chile

¹⁴Centro de Astrofísica y Tecnologías Afines (CATA), Casilla 36-D, Santiago, Chile

¹⁵Instituto de Astronomía, Universidad Católica del Norte, Angamos 0610, 1270709 Antofagasta, Chile

Accepted 2021 May 18. Received 2021 May 14; in original form 2021 April 14

ABSTRACT

We present the discovery of NGTS-19b, a high-mass transiting brown dwarf discovered by the Next Generation Transit Survey. We investigate the system using follow-up photometry from the South African Astronomical Observatory, as well as sector 11 *Transiting Exoplanet Survey Satellite* data, in combination with radial velocity measurements from the CORALIE spectrograph to precisely characterize the system. We find that NGTS-19b is a brown dwarf companion to a K-star, with a mass of $69.5^{+5.7}_{-5.4} M_{\text{Jup}}$ and radius of $1.034^{+0.055}_{-0.053} R_{\text{Jup}}$. The system has a reasonably long period of 17.84 d, and a high degree of eccentricity of $0.3767^{+0.0061}_{-0.0061}$. The mass and radius of the brown dwarf imply an age of $0.46^{+0.26}_{-0.15}$ Gyr, however, this is inconsistent with the age determined from the host star spectral energy distribution, suggesting that the brown dwarf may be inflated. This is unusual given that its large mass and relatively low levels of irradiation would make it much harder to inflate. NGTS-19b adds to the small, but growing number of brown dwarfs transiting main-sequence stars, and is a valuable addition as we begin to populate the so-called brown dwarf desert.

Key words: techniques: photometric – techniques: radial velocities – brown dwarfs.

1 INTRODUCTION

Brown dwarfs are substellar mass objects that bridge the gap between planets and stars. These are objects with radii similar to that of

Jupiter, but with masses ranging between 13 and $\sim 80 M_{\text{Jup}}$ (Baraffe et al. 2002; Spiegel, Burrows & Milsom 2011). The lower mass limit corresponds to the minimum mass at which deuterium burning can occur, below which lie the planets. Whilst the upper mass limit is the classical hydrogen-burning limit, above which objects are considered to be low-mass stars.

The first unambiguous detections of brown dwarfs were the discoveries of Gilese 229B (Nakajima et al. 1995) and Teide 1 (Rebolo, Zapatero Osorio & Martín 1995). Since then, there have

* E-mail: ja466@le.ac.uk

† Winton Fellow.

‡ Juan Carlos Torres Fellow.

been thousands of brown dwarfs discovered, the vast majority of which are isolated objects discovered by wide-field photometric surveys (e.g. Pinfield et al. 2008; Folkes et al. 2012; Reyl e 2018; Meisner et al. 2020; Schneider et al. 2020). This is a result of the fact that brown dwarfs cool as they age, due to a lack of nuclear fusion in their cores, making them much easier to detect at the long wavelengths that these surveys typically operate (e.g. *WISE*; Wright et al. 2010).

Not all brown dwarfs exist in isolated systems. Many have been discovered as companions to main-sequence stars, a large number of which have been identified via direct imaging (Nielsen et al. 2019; Vigan et al. 2020). However, brown dwarfs are much fainter than stars, and thus we can only resolve them at large orbital separations. To find close-in brown dwarfs, we need to look at the effect they have on their host star (e.g. via transits or radial velocity measurements).

In recent years, there have been an increasing number of transiting brown dwarfs discovered around main- and pre-main-sequence stars by exoplanet surveys (e.g. Csizmadia et al. 2015; Bayliss et al. 2017; Jackman et al. 2019). Given their Jovian sized radii, we would expect these objects to be easy to detect given the vast number of known hot Jupiters around main-sequence stars. Similarly, their large masses result in easy to detect radial velocity shifts (km s^{-1} scale rather than m s^{-1} for planetary mass objects) that should also aid in discovery. However, despite this, there are just 28 known transiting brown dwarfs around main-sequence stars (Carmichael et al. 2021; Palle et al. 2021), an unusually small number given the fact there are over 4000 known exoplanets.¹

This phenomenon is known as the brown dwarf desert (e.g. Grether & Lineweaver 2006) and was identified as being a dearth of brown dwarfs orbiting main-sequence stars within 3 au, in contrast to the large number of binary stars with close orbits (Marcy & Butler 2000). This was further highlighted by the discovery of large numbers of exoplanets in short-period orbits (\sim days), but very few brown dwarfs (Cumming et al. 2008). Recent work with SuperWASP confirmed that this desert still remains (Triaud et al. 2017), despite the vast number of transiting objects discovered by *Kepler* (Borucki et al. 2010) and *Transiting Exoplanet Survey Satellite (TESS)* (Ricker et al. 2015). The desert is thought to be a result of the differences between formation mechanisms for planets and brown dwarfs, although recent transiting brown dwarf discoveries have called into question the nature of this so-called desert (Carmichael, Latham & Vanderburg 2019).

Due to their scarcity, it is important that we understand and characterize those transiting brown dwarfs that have been discovered, in particular their masses and radii. Here, transiting brown dwarfs around main-sequence stars provide us with an advantage over isolated field brown dwarfs. Their radii can be measured from the depth of their transit in the light curve of their host star, whilst their masses can be measured using radial velocity measurements. Provided the host star parameters are well defined, this allows for accurate determination of these fundamental parameters.

These parameters are particularly valuable when combined with an accurate measurement of system age. As their masses are too small to fuse hydrogen, brown dwarfs cool and undergo gravitational contraction as they age. This contraction occurs most quickly up to an age of 1 Gyr and gradually decreases with time (Baraffe et al. 2003; Saumon & Marley 2008; Burrows, Heng & Nampaisarn 2011; Phillips et al. 2020). With knowledge of the age, we can compare the radius of the brown dwarf to that expected by models of gravitational

contraction (e.g. Phillips et al. 2020). Equally, we can use a well-defined mass and radius measurement to estimate the age of the brown dwarf, by comparing it with stellar isochrones of a variety of ages to see which provides the best fit.

However, whilst there are a large number of known brown dwarfs in stellar clusters with well-defined ages (Pearson et al. 2020), this is not the case for transiting brown dwarfs. There are very few with accurate age measurements as a result of cluster association (e.g. Gillen et al. 2017; Beatty et al. 2018; David et al. 2019). So the age often needs to be inferred by some other means, for example, through fitting the spectral energy distribution (SED) of the host star (Choi et al. 2016) or using stellar evolutionary tracks. However, this can result in uncertainties of up to a few Gyr in some cases (e.g. Bayliss et al. 2017; Nowak et al. 2017).

Age measurements are particularly important in the case of transiting brown dwarfs, as we are able to compare the brown dwarf masses and radii to evolutionary models (e.g. Baraffe et al. 2003; Marley et al. 2018). This is one of the best ways to compare the accuracy of these models, as we are comparing them to brown dwarfs whose properties have been directly measured from their interaction with their host stars, allowing for an improved understanding of how these objects evolve as they age. This is particularly important at the high-mass ($60\text{--}80 M_{\text{Jup}}$) end of the distribution, where Baraffe et al. (2003) predict the largest changes in radii with age.

It is well established that low-mass stars in eclipsing binaries show significant scatter in the relationship between mass, radius, and luminosity when compared with evolutionary models (Parsons et al. 2018). However, with so few transiting brown dwarfs yet discovered, whether this relationship continues into the substellar regime is unclear. It has been suggested that brown dwarfs may be able to be inflated if they orbit host stars that are particularly active (Casewell et al. 2020). A comparison with evolutionary models would suggest that high-mass brown dwarfs are much less likely to be inflated, regardless of the effect of their host star. Additionally, detailed investigation of individual systems has shown that stellar irradiation alone cannot explain discrepancies when they are observed (Beatty et al. 2018). However, with so few transiting brown dwarfs known it is challenging to make any clear determination of the cause of these discrepancies. Hence, it is important that we discover and characterize as many of these systems as possible.

In this paper, we present the discovery of NGTS-19b, a high-mass brown dwarf in an eccentric 17-d orbit around a main-sequence K-star. We make use of high-precision photometric and spectroscopic follow up to derive an accurate mass and radius for the brown dwarf. We then place this system in the context of the growing number of brown dwarfs being identified around main-sequence stars, and explain how this, and future discoveries will aid in understanding the formation and evolution of these systems.

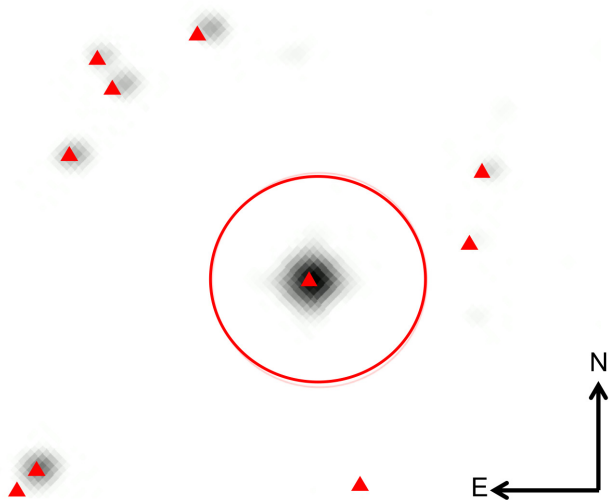
2 OBSERVATIONS

NGTS-19 was initially discovered using photometry from the Next Generation Transit Survey (hereafter NGTS; Wheatley et al. 2018). Follow-up observations were performed with the Sutherland High Speed Optical Cameras (SHOC; Coppejans et al. 2013) on the South African Astronomical Observatory (SAAO) 1-m telescope. This photometry was then used in conjunction with observations from the *TESS* (Ricker et al. 2015). We obtained high-resolution spectra with the CORALIE spectrograph (Queloz et al. 2000) to determine the mass of the companion. These observations are detailed in Table 1 and described below.

¹According to the NASA Exoplanet Archive, 2021 March.

Table 1. Summary of photometric and spectroscopic observations of NGTS-19.

Observation type	Telescope	Band	Cadence	Total integration time	Period	Notes
Photometry	NGTS	520–890 nm	13 s	148 nights	26-01-17–17-09-17	Three transits
Photometry	SAAO	V	60 s	400 min	19-07-20	Single observation
Photometry	<i>TESS</i>	600–1000 nm	1800 s	28 d	22-04-19–20-05-19	Two transits
Spectroscopy	CORALIE	390–680 nm	45 min	4.5 h	05-02-20–27-02-21	Eight RVs

**Figure 1.** Digital Sky Survey image of NGTS-19. The red triangles indicate the positions of nearby objects that are identified in *Gaia* DR2. The red circle shows the NGTS aperture used to create the NGTS light curve. NGTS-19 is the only known source within the aperture used for reduction.

2.1 NGTS photometry

Transits of NGTS-19b were initially detected in survey photometry from the NGTS (Wheatley et al. 2018). NGTS is a wide-field ground-based survey for transiting exoplanets operating at ESO’s Paranal observatory in Chile. It consists of an array of 12 fully automated 20 cm telescopes that operate independently to survey large areas of the sky each night. NGTS is optimized for observations of K- and M-type stars, with a custom bandpass range of 520–890 nm. NGTS has a wide field of view (instantaneously covering 96 deg²) and delivers high-cadence (every ~13 s) photometry with high precision (1 mmag per hour for an $I = 14$ mag star).

NGTS-19 was observed during the 2017 NGTS observing season. The field containing the system (NG1518–2518) was observed for 148 nights between 2017 January 26th and 2017 July 17th, and in total we obtained 200 547 science images at a cadence of 13 s. The star is shown in Fig. 1. The star is well isolated, and there are no additional *Gaia* DR2 sources in the NGTS aperture that could dilute the depth of the transit. We also note that none of the nearby *Gaia* DR2 sources have a parallax or proper motion that is consistent with being physically associated with NGTS-19. The magnitudes of the system in various bandpasses, as well as positional information, are provided in Table 2.

The raw light curve was cleaned using an implementation of the SYSREM algorithm (Tamuz, Mazeh & Zucker 2005). Transits were then detected using the ORION algorithm, which is a custom implementation of the usual boxed least-squares (BLS; Kovács, Zucker & Mazeh 2016) algorithm (see e.g. Wheatley et al. 2018, for more information).

Table 2. Stellar properties and colour magnitudes for NGTS-19 from 2MASS (Skrutskie et al. 2006), *Gaia* (Gaia Collaboration 2018), TICv8 (Stassun et al. 2019), and NGTS (Wheatley et al. 2018).

Property	Value	Source
<i>Gaia</i> ID	DR2 6226795997504049664	<i>Gaia</i>
TIC ID	48481940	TIC v8
RA (J2000)	15:16:31.6	NGTS
Dec. (J2000)	−25:42:17.24	NGTS
μ_α (mas yr ^{−1})	−45.796 ± 0.054	<i>Gaia</i>
μ_δ (mas yr ^{−1})	−14.746 ± 0.038	<i>Gaia</i>
Parallax (mas)	2.6666 ± 0.0285	<i>Gaia</i>
<i>G</i>	13.83	<i>Gaia</i>
NGTS	13.20	NGTS
<i>TESS</i>	13.20	TIC v8
<i>B</i>	15.18	TIC v8
<i>V</i>	14.12	2MASS
<i>J</i>	12.27	2MASS
<i>H</i>	11.82	2MASS
<i>K</i>	11.70	2MASS

The NGTS observations captured three transits of the system (see Fig. 2). From this, ORION detected an orbital period of 17.8 d and transit depth of around 1.5 per cent, corresponding to an object with a radius approximately that of Jupiter. Any shorter period alias could be ruled out by the lack of detection on other nights the star was observed. NGTS candidates are also vetted by a convolutional neural network (CNN) designed to distinguish between transiting signals and false positives (Chaushev et al. 2019). NGTS-19 received a CNN probability of 0.96, strongly suggesting the detection was from a transiting planetary-sized object. This information gave us good confidence that the signal was real, and we decided to undertake follow-up observations.

2.2 TESS photometry

NGTS-19 was observed by *TESS* in Sector 11 of the primary mission (TIC-48481940, $T = 13.2$ mag). The system was observed between 2019 April 22nd and 2019 May 20th, in the full-frame images at 30 min cadence. *TESS* observed NGTS-19 with CCD 3 of camera 1.

To extract the light curve of NGTS-19 from the full-frame images, we used a bespoke process, described in more detail in Gill et al. (2020). In short, we use a custom aperture that is selected based on a flux threshold. Background pixels were selected using an iterative sigma clipping process, and pixels where the median counts exceeded 100 times the standard deviation in the background were identified as the source. We then used a floating median to identify and mask out systematic flux drops due to spacecraft effects.

TESS detects two transits of NGTS-19 spaced approximately 17-d apart (see Fig. 2). It is worth noting that the *TESS* observations alone cannot rule out the orbital period of the system being half of this, as a third transit would fall in the data gap in the middle of the sector during spacecraft downlink. However, this potential shorter period is not compatible with either the NGTS photometry (Section 2.1)

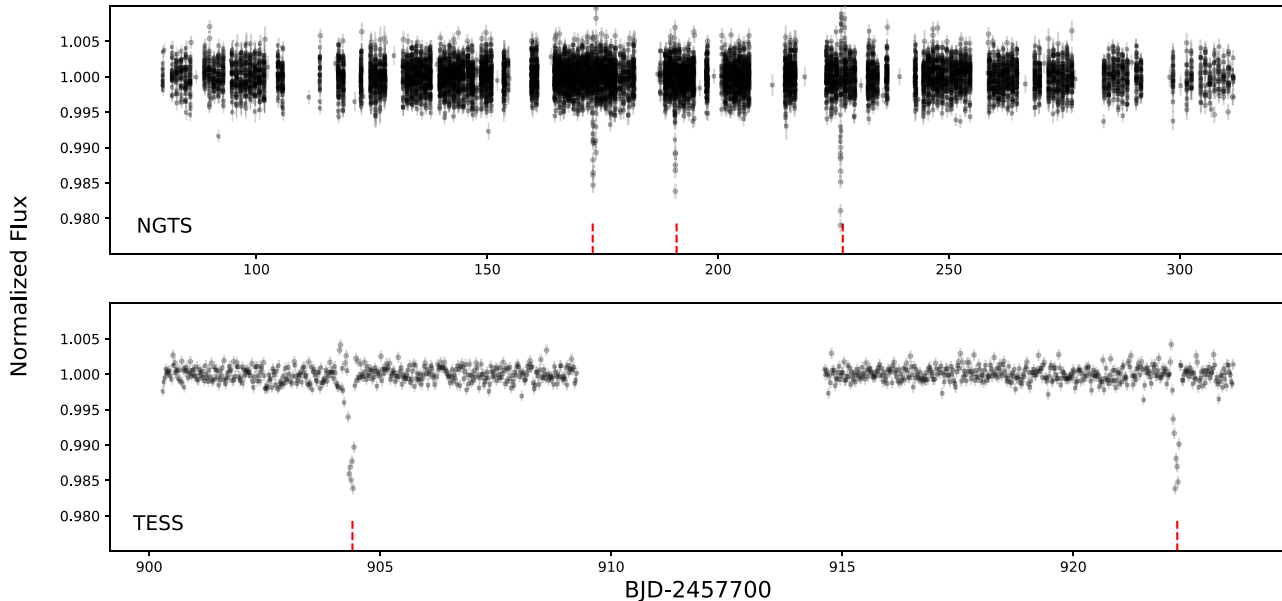


Figure 2. Upper: NGTS light curve of NGTS-19 comprising of 148 nights of observations, binned to 5 min. NGTS detects three transits of the system, indicated by the red lines. Lower: *TESS* light curve for NGTS-19 obtained during sector 11 of the mission (TIC-48419840), observed at 30 min cadence in full-frame images. Two transits are seen during the sector, spaced approximately 17.8 d apart, and are indicated by the red dashed line.

or the radial velocity measurements (Section 2.4), which are both compatible with a 17.8-d period, thus highlighting the need for additional data to interpret the *TESS* photometry. We note that NGTS-19 will be re-observed in *TESS* sector 38 of the extended mission. Based on our established ephemeris, *TESS* should then observe a further two transits.

2.3 SAAO photometry

Due to the period of this system, the combined photometry of NGTS and *TESS* contained only a small number of transits. Thus, we obtained additional photometry of NGTS-19 using the 1-m telescope at SAAO with the SHOC instrument on 2020 July 19th. This would allow us to obtain more precise measurements of the transit depth and width, and thus increase our precision on the radius of the companion. We observed the transit in the *V* band in order to check for any colour-dependent depth difference that may be indicative of a stellar companion. The observation consisted for 400×60 -s exposures for a total observation time of 6 h 40 min.

The data were bias and flat-field corrected via the standard procedure, using the SAFPHOT PYTHON package.² SAFPHOT was also used to carry out differential photometry, by extracting aperture photometry from the target as well as comparison stars using the ‘SEP’ package (Barbary 2016). SEP also measured and subtracted the sky background, adopting a box size and filter width that minimized the background residuals measured across the frame after the stars had been masked out. Two comparison stars were used to perform differential photometry on the target, with a 3.8 pixel radius aperture selected to maximize the signal-to-noise ratio.

The observation clearly detects the transit, which occurred almost exactly as predicted by the ephemeris from the NGTS and *TESS* observations. We also note no significant difference in depth between this light curve and the NGTS and *TESS* observations, despite the

fact the SAAO data were obtained using a much bluer filter. This adds further confidence to the companion being substellar in nature.

2.4 CORALIE radial velocities

To determine the mass and orbital eccentricity of NGTS-19b, we obtained spectroscopic observations using the CORALIE spectrograph mounted on the Swiss 1.2-m Leonhard Euler Telescope at ESO’s La Silla Observatory, Chile. CORALIE is an Echelle spectrograph fed by a 2 arcsec science fibre, capable of 3 m s^{-1} radial velocity precision on bright stars (see e.g. Rickman et al. 2019, for recent results). As NGTS-19 is relatively faint for a telescope of this size ($V = 14.12$), we used long (45 min) exposures to maximize the signal-to-noise ratio. This allowed for precision on a scale of around 100 m s^{-1} , which is sufficient to distinguish between stellar and substellar companions.

We obtained a total of eight spectra of NGTS-19. These were cross-correlated with a binary G2 mask using the standard CORALIE pipeline, while discarding the first 20 spectral orders where the signal-to-noise ratio was less than one. The radial velocity associated with NGTS-19 was extracted from the cross-correlation function by fitting a Gaussian function. The radial velocity measurements show a large amplitude variation ($\sim 6.5 \text{ km s}^{-1}$) in phase with the period defined by the NGTS photometry, with a significant level of eccentricity. This suggests the presence of a high-mass substellar companion. The full radial velocity measurements are shown in Table 3. We note that one of the points was obtained close to phase 0, however, we ensured that this measurement was not taken during the transit of the brown dwarf.

3 ANALYSIS

3.1 Spectral analysis

We used the CORALIE spectra of NGTS-19 to obtain initial parameters for the system. The CORALIE spectra were shifted

²<https://github.com/apchsh/SAFPhot>

Table 3. Radial velocities for NGTS-19 obtained with the CORALIE spectrograph.

BJD _{TDB}	RV	RV error	FWHM	Contrast	Bisector span
(−2450000)	(km s ^{−1})	(km s ^{−1})	(km s ^{−1})	(per cent)	
8884.876	−30.53	0.17	9.68	53.50	−0.097
8885.832	−26.50	0.13	9.57	53.28	−0.239
8903.859	−26.15	0.14	9.43	54.37	0.057
8911.851	−36.73	0.11	9.82	49.47	−0.299
8925.753	−32.27	0.11	9.15	52.78	0.0212
8928.730	−36.14	0.15	9.01	54.19	−0.014
9261.805	−25.77	0.14	9.25	58.78	−0.17
9272.782	−38.40	0.16	9.14	52.94	−0.28

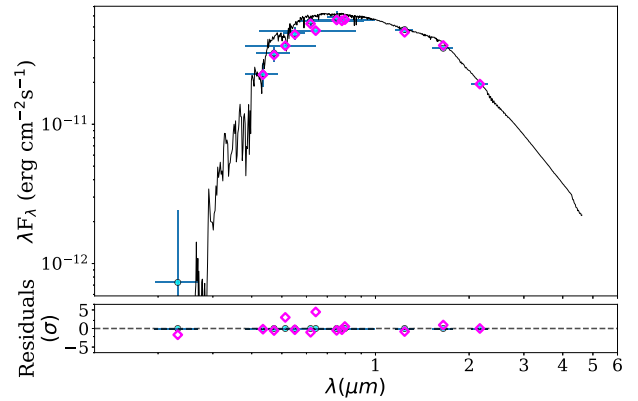
Table 4. NGTS-19 stellar parameters derived using SPECMATCH-EMP and ARIADNE. The ARIADNE parameters are used for the global modelling of the system in Section 3.3.

Parameter	SPECMATCH-EMP	ARIADNE
T_{eff} (K)	4500 ± 110	4716^{+39}_{-28}
$\log g$ (cm s ^{−2})	4.62 ± 0.12	$4.571^{+0.102}_{-0.093}$
Radius (R_{\odot})	0.71 ± 0.10	$0.896^{+0.040}_{-0.035}$
[Fe/H]	0.09 ± 0.09	$0.11^{+0.074}_{-0.070}$
Mass (M_{\odot})	0.73 ± 0.08	$0.807^{+0.038}_{-0.043}$
Age (Gyr)	–	$8.5^{+3.2}_{-6.0}$
Distance (pc)	–	371^{+15}_{-12}

in wavelength and co-added to create a single high-signal-to-noise spectrum for spectral analysis. However, owing to the faintness of the system this combined spectrum still had a relatively low signal-to-noise ratio (8.28). None the less, it was sufficient to obtain some initial system parameters that would be refined in the subsequent analysis.

We analysed this stacked spectrum using the template matching code SPECMATCH-EMP (Yee, Petigura & von Braun 2017), which characterizes spectra of stars by comparing them with a library of high-resolution spectra obtained with Keck/HIRES. SPECMATCH-EMP first shifts the input spectrum to the same wavelength scale as the templates, and then compares it to each star in the library to find the best-matching individual spectra. Linear combinations of the best matches are then used to create the best match to the input spectrum. Various stellar parameters for the star are then computed based on a weighted average of library parameters from the reference spectra. These properties are shown in Table 4. The parameters calculated by SPECMATCH-EMP show that the star is a late K-dwarf with a mass of $0.73 M_{\odot}$. Rather than adopting these as the final parameters for the primary star, we use them as priors for the SED fitting procedure detailed in Section 3.2.

It is interesting to note, that from this analysis we constrain the metallicity to a value of $+0.1$ dex, implying that NGTS-19 is a metal-rich star. Even though in Jenkins et al. (2015) they show that the median brown dwarf host star metallicity is subsolar, the distribution spans a wide range of values with a flat functional form, unlike the case of giant planets. Here, NGTS-19 adds another example to the metal-rich population of brown dwarf host stars, and this time with a measured radius.


Figure 3. Upper panel: SED of NGTS-19. Blue points show the catalogue photometry for the system from a variety of sources, and the magenta diamonds are the synthetic photometry fit. The black line shows the best-fitting model. Lower panel: Residuals to the SED fit, normalized to the photometry errors.

Additionally, we used this stacked spectrum to determine the projected stellar rotation velocity ($v \sin(i)$). To do this, we fit synthesized spectra to the spectrum of NGTS-19 using iSpec (Blanco-Cuaresma et al. 2014). We fit only for $v \sin(i)$, fixing the other values to those obtained from SPECMATCH-EMP. From this, we obtain a value for $v \sin(i)$ of 2.1 ± 0.4 km s^{−1}.

3.2 SED fitting

To obtain precise parameters for the host star, we performed a fit to the SED. This was done using ARIADNE (Vines & Jenkins, in preparation), which we describe in brief here. ARIADNE is a publicly available PYTHON tool that fits catalogue photometry of stars from various sources (e.g. *Gaia*, *TESS*) to various atmospheric model grids. The specific grids used by ARIADNE are Phoenix v2 (Husser et al. 2013), BT-Settl, BT-Cond, BT-NextGen (Hauschildt, Allard & Baron 1999; Allard, Homeier & Freytag 2012), as well as the grids of Castelli & Kurucz (2004) and Kurucz (1993).

We create model SEDs by interpolating these grids in $T_{\text{eff}}-\log g$ -[Fe/H] space, with distance, radius, and extinction in the V band used as model parameters. An excess noise term was applied for each set of parameters to account for an underestimation of the uncertainties. These were normally distributed around zero with a variance of five times the size of the reported uncertainty. Priors for T_{eff} , $\log g$, [Fe/H], and radius were applied based on the results from SPECMATCH-EMP (see Section 3.1). Extinction was limited to the maximum line-of-sight value taken from the Schlegel, Finkbeiner & Davis (SFD) Galactic dust map (Schlegel, Finkbeiner & Davis 1998; Schlafly & Finkbeiner 2011).

The parameters from the SED were estimated using nested sampling performed using the PYTHON package DYNESTY. This was also used to calculate the Bayesian evidence for each of the individual models. For the fitted parameters, a weighted average is then computed using the relative probabilities of each of the fitted models. This Bayesian model averaging results in a remarkable degree of precision in these parameters when compared with using any one individual model SED fit. Finally, a mass estimate is calculated using a MIST isochrone (Choi et al. 2016). The results of this fitting are given in Table 4, and the fit to the SED is shown in Fig. 3. Based on our SED fit and the classification established by Pecaut & Mamajek

(2013), this makes the primary star a K3.5V dwarf. We adopt these parameters for the host star in our subsequent global fitting for this system

3.3 Global modelling

To determine orbital parameters for the system, we jointly modelled the photometry and radial velocities using ALLESFITTER (Günther & Daylan 2019, 2021). ALLESFITTER is a publicly available PYTHON code for performing global modelling of photometric and radial velocity data. The software acts as a wrapper for a number of well-used packages, in particular, we utilize the eclipsing binary light-curve modeller ELLC (Maxted 2016) and the Markov chain Monte Carlo (MCMC) sampler EMCEE (Foreman-Mackey et al. 2013) to simultaneously model the NGTS, *TESS*, SAAO, and CORALIE data. Prior to running the MCMC, we perform some simple preparation of the data. The raw light curves were normalized to a baseline of 1 by using the median out-of-transit flux. We then binned the NGTS data to 10 min, to reduce computational time. The *TESS* and SAAO data remained unbinned.

We chose to start the walkers in a region of parameter space that gave a reasonable initial fit to the data. We note that whilst starting the walkers in a random position does not preclude the ability to obtain a good fit to the data, it does increase the burn-in time required to do so. Each walker was given a starting position normally distributed around the values we found to give an initial fit. We used values from ORION for the ephemeris of the system, and obtained values for the stellar radius ratio, scaled primary star radius, and inclination from an initial fit of the NGTS data alone performed by ORION. Equally, starting positions for the radial velocity parameters were determined by fitting these data alone. We also incorporated a radial velocity jitter term in quadrature to account for any effects of stellar variability in the RVs, as well as normalization offsets and systematic errors for the light curves. We knew from the radial velocity measurements that there was a significant level of eccentricity in the system, but for the fitting we started the walkers at zero eccentricity and allowed the sampler to determine it. We note that for fitting purposes, ALLESFITTER parametrizes eccentricity (e), relative to the argument of periastron (ω), using terms $\sqrt{e}\cos(\omega)$ and $\sqrt{e}\sin(\omega)$. Finally, we also determined limb darkening parameters using the LDTK package (Parviainen & Aigrain 2015) for each photometric filter used, adopting limb darkening laws from Kipping (2013) in the fit.

We ran ALLESFITTER with 100 walkers going for 80 000 steps. We found this to be more than sufficient for the MCMC to converge to a solution, ensuring that the chains were at least 30 times the autocorrelation length of each parameter. 10 000 of these steps were discarded as burn in and not used when analysing the results. The modal values of the posterior distributions for each parameter were adopted as the most probable values, with the 1σ (68.3 per cent) confidence intervals taken as an estimate of uncertainty. The fitted parameters were then used to derive additional parameters for the system.

This global modelling reveals the companion in this system is a high-mass brown dwarf, with a mass of $69.5^{+5.7}_{-5.4} M_{\text{Jup}}$ and radius of $1.034^{+0.055}_{-0.053} R_{\text{Jup}}$. The system is also notable for having a reasonably long period of $17.839654^{+0.000037}_{-0.000038}$ d, and a high level of eccentricity $0.3767^{+0.0061}_{-0.0061}$. We note that this period makes NGTS-19 the longest period transiting brown dwarf to be initially discovered using purely ground-based photometry, highlighting the value of the long observing baselines used by NGTS. The full list of fitted and derived parameters for the system is given in Table 5. The model fits to each set of data are shown in Figs 4 and 5.

Table 5. Best-fitting and derived parameters from the global modelling of NGTS-19 using ALLESFITTER. The values are derived from the modal values of the posterior distribution, with 1σ uncertainties stated as errors. Note that the limb darkening coefficients are parametrized as in Kipping (2013).

Parameter	Symbol	Unit	Value
Fitted transit parameters			
Scaled BD and star radii	$(R_* + R_{\text{BD}})/a$	–	$0.0359^{+0.0015}_{-0.0013}$
Radius ratio	R_{BD}/R_*	–	$0.1182^{+0.0037}_{-0.0035}$
Cosine inclination	$\cos i$	–	$0.0223^{+0.0018}_{-0.0019}$
Impact parameter	b	–	$0.730^{+0.033}_{-0.041}$
Epoch	T_0	HJD	$2458533.0207^{+0.0011}_{-0.0011}$
Period	P	d	$17.839654^{+0.000037}_{-0.000038}$
$\sqrt{e}\cos(\omega)$	f_c	–	$0.5322^{+0.0042}_{-0.0042}$
$\sqrt{e}\sin(\omega)$	f_s	–	$-0.306^{+0.014}_{-0.014}$
Limb darkening parameters			
NGTS LDC 1	$q_{1,\text{NGTS}}$		$0.64^{+0.22}_{-0.24}$
NGTS LDC 2	$q_{2,\text{NGTS}}$		$0.53^{+0.27}_{-0.29}$
TESS LDC 1	$q_{1,\text{TESS}}$		$0.37^{+0.25}_{-0.18}$
TESS LDC 2	$q_{2,\text{TESS}}$		$0.39^{+0.32}_{-0.25}$
SAAO LDC 1	$q_{1,\text{SAAO}}$		$0.37^{+0.29}_{-0.21}$
SAAO LDC 2	$q_{2,\text{SAAO}}$		$0.45^{+0.31}_{-0.28}$
Radial velocity parameters			
Systemic velocity	V_{sys}	km s ⁻¹	$-33.9166^{+0.0097}_{-0.0105}$
RV semi-amplitude	K	km s ⁻¹	$6.492^{+0.063}_{-0.062}$
Derived brown dwarf parameters:			
Brown dwarf mass	M_{BD}	M_{Jup}	$69.5^{+5.7}_{-5.4}$
Brown dwarf radius	R_{BD}	R_{Jup}	$1.034^{+0.055}_{-0.053}$
Brown dwarf density	ρ_{BD}	g cm ⁻³	77^{+17}_{-13}
Semimajor axis	a	au	$0.1296^{+0.0074}_{-0.0072}$
Scaled semimajor axis	a/R_*	–	$27.9^{+1.6}_{-1.6}$
Inclination	i	deg	$88.72^{+0.11}_{-0.11}$
Orbital eccentricity	e	–	$0.3767^{+0.0061}_{-0.0061}$
Argument of periastron	ω	deg	$330.1^{+1.4}_{-1.3}$
Equilibrium temperature	$T_{\text{eq,BD}}$	K	543^{+17}_{-16}
Transit duration	t_{trans}	h	$4.252^{+0.077}_{-0.074}$

4 DISCUSSION

4.1 Mass–radius relation

In Section 3.3, we determined that the companion to NGTS-19 is a high-mass brown dwarf. This adds to the small, but growing number of objects being discovered in the so-called brown dwarf desert. With direct measurements of the brown dwarf’s mass and radius, we can make a comparison with both the known population of transiting brown dwarfs, as well as with predictions from evolutionary models. In Fig. 6, we compare the mass and radius of NGTS-19b to the known brown dwarf companions around main-sequence stars from Carmichael et al. (2021). We see that with a mass of $69.5^{+5.7}_{-5.4} M_{\text{Jup}}$, NGTS-19b lies at the upper end of the brown dwarf mass distribution, close to the substellar boundary.

When we compare the system to isochrones from Marley et al. (2018), we see that the system agrees well with the 0.4 Gyr model. This is in contrast to the age determination from the SED fit performed by ARIADNE, which predicted a much older system age of $8.5^{+3.2}_{-6.0}$ Gyr. This leaves us with two potential scenarios. It is possible that the system is indeed young, despite the age estimates from the SED. Alternatively, we may assume that the age from the SED fit

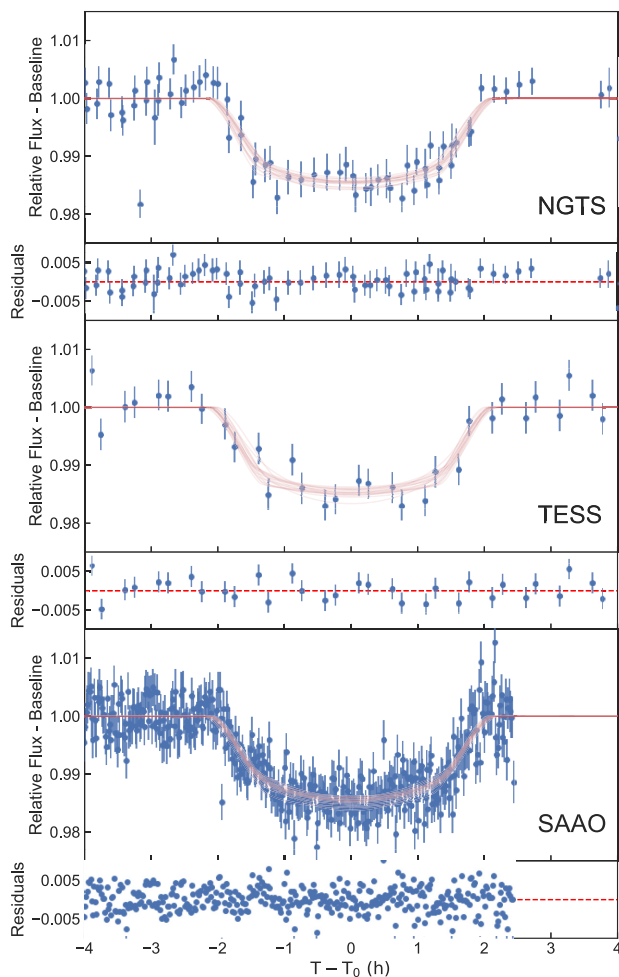


Figure 4. Data and model fits to the photometry from NGTS, *TESS*, and SAAO 1 m obtained using ALLESFITTER. The NGTS data are binned to 10 min, whereas the *TESS* and SAAO data are unbinned. The red line shows the model fit derived by ALLESFITTER, and the shaded region is the uncertainty in the model.

is correct and the brown dwarf’s radius has been inflated by some mechanism, making it appear younger in mass–radius space.

4.1.1 Possible youth of the system

An important parameter to know for any discovered transiting brown dwarf is the system age. To gain some estimate of this, we compare the mass and radius of NGTS-19b to evolutionary models from a variety of ages. We follow the method of Gillen et al. (2020), first interpolating between the models in order to compute a finer grid of model predictions and then comparing our global modelling results for the mass and radius of the system to this grid to compute an age estimate. For this, we use the Sonora brown dwarf models of Marley et al. (2018). Doing so yields an estimate for the age of the system of $0.46^{+0.26}_{-0.15}$ Gyr; this is not consistent with the determined age from ARIADNE, which predicts an older system.

Despite the small number of transiting brown dwarfs yet discovered, there are a reasonable number of young systems. These are often found in clusters, from which the age can be accurately determined (Gillen et al. 2017; Beatty et al. 2018; David et al. 2019). However,

there are known brown dwarfs orbiting young stars not associated with clusters, for example, NGTS-7Ab (Jackman et al. 2019), with an age of just 55 Myr. Discoveries of brown dwarfs at these ages are important, as they will be undergoing gravitational contraction at a faster rate than at later ages (as seen by the large gaps between isochrones in Fig. 6). This allows for some of the most powerful tests of brown dwarf evolutionary models.

This, however, does not explain the discrepancy seen between the age determined from the brown dwarf mass and radius, and that found in the SED fit. We note that the age determined from the SED by ARIADNE is poorly constrained, and is consistent with our inferred brown dwarf age at the 2σ level. To try and confirm or refute this age measurement, we checked for additional youth indicators. We examined the CORALIE spectrum for signs of Lithium absorption, which is typically an indicator of youth, however, we find no such absorption in the spectrum. The star also has a relatively low $v\sin(i)$, which would also not suggest youth, and is not part of a known moving group. Thus, the only evidence that the brown dwarf is young is its unusually large radius. This means that we cannot conclusively say that this is indeed a young system, as the radius of the brown dwarf could have been increased by some other means.

4.1.2 Inflated brown dwarf radii

It should be noted, however, that the models used in Fig. 6 are for isolated brown dwarfs, whereas here we have a brown dwarf with a close stellar companion. Therefore, it is possible that the system is indeed the age determined from the SED, and NGTS-19b is inflated relative to model predictions. There are brown dwarfs with unusually large radii, however, these are usually associated with being strongly irradiated (e.g. Siverd et al. 2012; Zhou et al. 2019), although this is not always the case (e.g. Csizmadia et al. 2015).

Bouchy et al. (2011) showed that unlike in the case of hot Jupiters, where stellar irradiation can play a large effect in inflating the radii of the companion (Sestovic, Demory & Queloz 2018), the effect is much smaller for brown dwarfs, particularly at the higher mass end. It is also worth noting that the brown dwarf they were analysing (CoRoT-15b) has an equilibrium temperature almost twice that of NGTS-19b. Hence, it is even less likely to have an effect on the radius of this system. In Fig. 7, we plot the relationship between the radius and equilibrium temperature for known brown dwarfs. We see that although there is perhaps a slight upwards trend in radius with increasing temperature, it is not noticeably significant. When compared to brown dwarfs with similar equilibrium temperatures, we see that the radius of NGTS-19b is not an outlier, and is well within the observed scatter. If NGTS-19b is truly an inflated brown dwarf, then there must be some other means to have increased its radius other than purely irradiation from its host star.

It is important to note, however, that the orbit of NGTS-19b is highly eccentric, and thus the distance between the brown dwarf and its host star varies significantly. Based on the measured eccentricity and semimajor axis, we determine a periastron distance of 0.0817 au, which is not too dissimilar to that of a hot Jupiter. Therefore, it is possible that the increased irradiation experienced by the brown dwarf at periastron could act to inflate its radius. This eccentric orbit could also act to inflate the brown dwarf due to tidal effects exerted on it by the host star, as has been demonstrated for gas giant exoplanets (Millholland, Petigura & Batygin 2020). However, given the long period of the system, and the high mass of the brown dwarf, we determine it to be unlikely that these effects would transfer enough heat into the brown dwarf to inflate it.

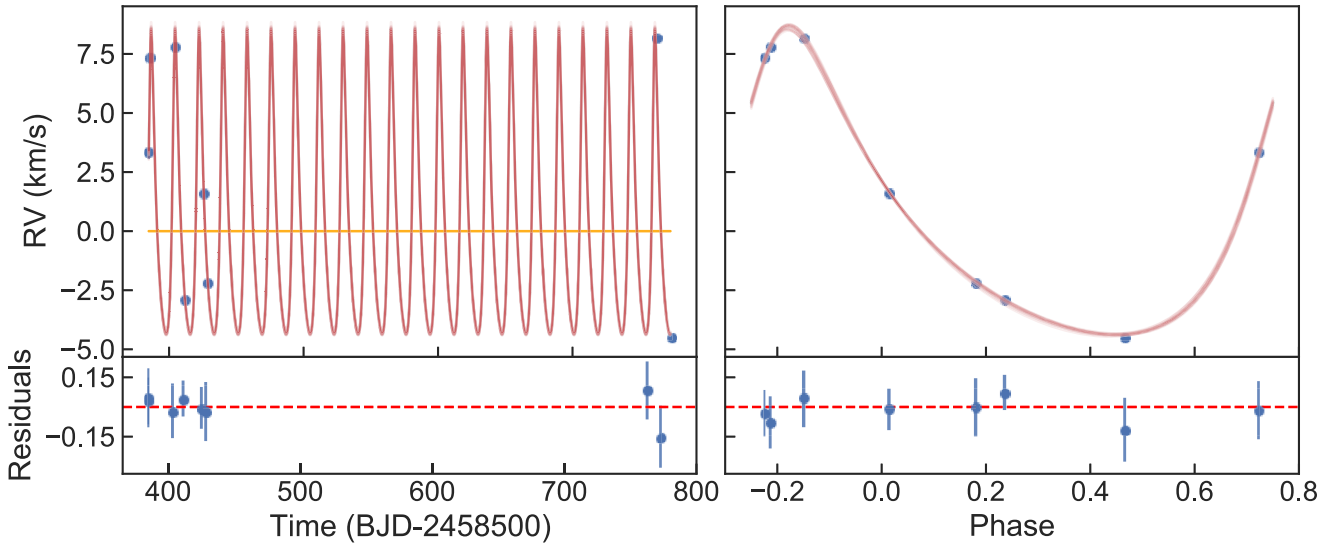


Figure 5. Data and model fits to the radial velocity measurements from CORALIE, obtained using ALLESFITTER. The CORALIE radial velocities have had the systemic velocity of the NGTS-19 system subtracted, and a jitter term has been added in quadrature to the error bars. The red line shows the model fit derived by ALLESFITTER, and the shaded region is the 1σ uncertainty in the model. The left-hand panel shows the measurements in time series, and the right-hand panel shows the radial velocities folded on the period determined by global modelling.

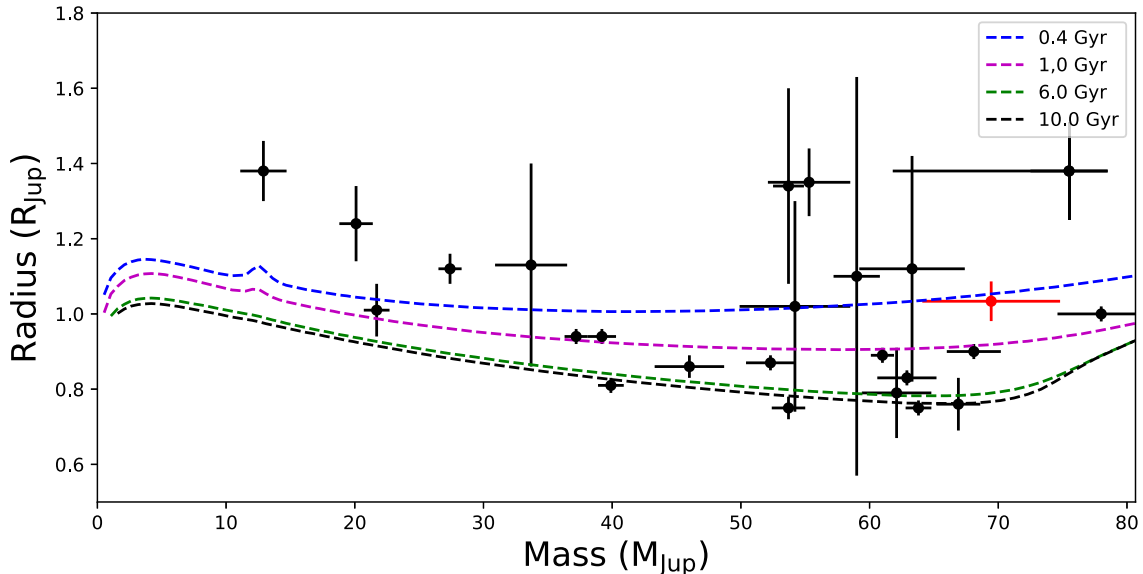


Figure 6. Mass–radius relation for known brown dwarfs around main-sequence stars from Carmichael et al. (2021). NGTS-19b is plotted in red. Sonora model isochrones from Marley et al. (2018) for ages of 0.4, 1, 6, and 10 Gyr are plotted for comparison. Note that neither RIK 72b (David et al. 2019) is shown due to its inflated radius of $3.1R_{\text{Jup}}$ nor is the brown dwarf binary system 2M0535–05a (Stassun, Mathieu & Valenti 2006).

Casewell et al. (2020) consider the white dwarf–brown dwarf binary NLTT5036, which also shows signs of inflation. They show that regardless of the level of irradiation experienced, low-mass brown dwarfs ($M < 35 M_{\text{Jup}}$) are able to be inflated when heated by their host star. However, higher mass brown dwarfs are much harder to inflate, with the majority of them showing no inflation. The temperature of the host star also plays an important role here: hotter stars will emit more ultraviolet radiation whereas cooler stars will emit more in the infrared. NGTS-19, a mid-K-dwarf, has an effective temperature of 4890 K that would leave it at the cooler end of the distribution of transiting brown dwarf host stars (Carmichael et al. 2021), with no significant amount of either UV or IR radiation.

Stellar activity may also affect the ability of a brown dwarf to be inflated by its host star. CoRoT-15b (Bouchy et al. 2011) and CoRoT-33b (Csizmadia et al. 2015) both show signs of being inflated, and are noted to be orbiting active host stars. This may suggest that brown dwarf inflation is caused by a similar mechanism to M-dwarfs (Stelzer et al. 2013). However, these two brown dwarfs both have large radii uncertainties (27 per cent and 48 per cent for CoRoT-15b and 33b, respectively) so it is difficult to categorically say whether or not these systems are actually inflated. We note that NGTS-19 does not show any signs of significant stellar activity. In almost 150 nights of NGTS data, we do not detect any obvious flares, and the CORALIE spectra do not show any signs of magnetic activity, such as

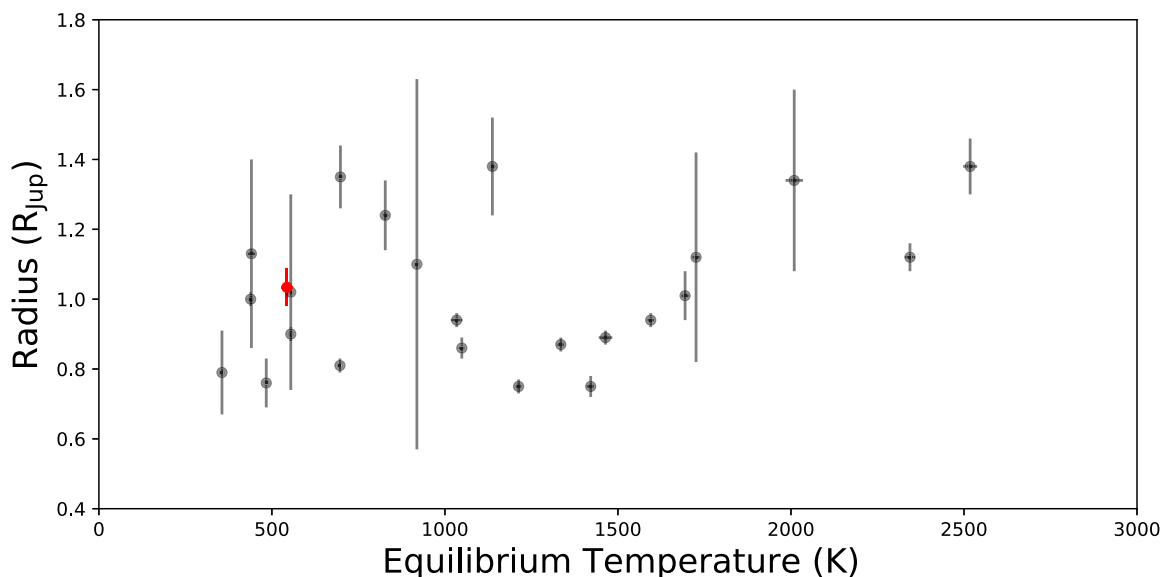


Figure 7. Relationship between equilibrium temperature and radius for known brown dwarfs around main-sequence stars from Carmichael et al. (2021). NGTS-19b is plotted in red. We use the effective temperature of the host star (if reported) and the relation in Méndez & Rivera-Valentín (2017) to calculate the time-averaged equilibrium temperature of the brown dwarf. For all systems, we assume a Bond albedo of zero. Note that neither RIK 72b (David et al. 2019) is shown due to its inflated radius of $3.1R_{\text{Jup}}$ nor is the brown dwarf binary system 2M0535–05a (Stassun et al. 2006).

$H\alpha$ emission. However, to accurately characterize the stars magnetic field would require further investigation.

Another important factor to consider is metallicity. For a fixed mass and age, the radii of brown dwarfs increase with increasing metallicity. Burrows et al. (2011) show that a change from +0.0 dex to +0.5 dex in the metallicity of the brown dwarf can result in an increase in radius of as much as $0.1 R_{\text{Jup}}$. Our analysis in Sections 3.1 and 3.2 suggest a small, but significant host star metallicity of around 0.1 dex. This may explain some of the discrepancy between model and measurement we see for NGTS-19b, but is unlikely to increase the radius by enough given the disagreement between our measured and predicted ages. They also show that differences between clear and cloudy brown dwarf models can cause deviations in radius by about $0.05 R_{\text{Jup}}$, but this too is likely not substantial enough to account for the discrepancy seen in our measurements.

4.2 Eccentricity and tidal circularization

NGTS-19b has a relatively large orbital eccentricity of $0.3767^{+0.0061}_{-0.0061}$ (Section 3.3). This is not necessarily unusual for transiting brown dwarfs. Of the 27 transiting brown dwarfs listed by Carmichael et al. (2021), 10 have eccentricity greater than 0.1. In Fig. 8, we show the distribution of eccentricity as a function of orbital period for the population of transiting brown dwarfs. Only two known systems have a higher eccentricity than NGTS-19b, these are TOI-811b and KOI-415b (Moutou et al. 2013; Carmichael et al. 2021) with orbital eccentricities of 0.4072 ± 0.046 and 0.689 ± 0.001 , respectively. However, with orbital periods of 25.2 and 166.8 d, these systems are both longer period than NGTS-19b and there is no known transiting brown dwarf with a shorter orbital period that has a higher degree of eccentricity.

For a system with a semimajor axis of just $0.1296^{+0.0074}_{-0.0072}$ au, this is a reasonably high level of eccentricity. It is known that over the course of evolution of such small separation systems, the tidal effect of the host star acts to circularize the orbit. This was a process first applied to binary stars (Zahn & Bouchet 1989), but is equally applicable to

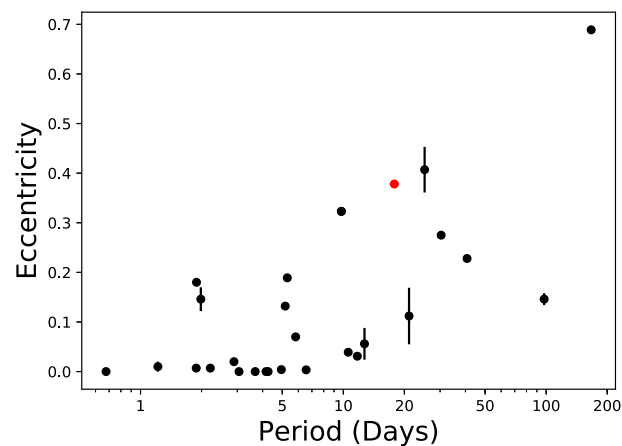


Figure 8. Eccentricity against period for known transiting brown dwarfs orbiting main-sequence stars from Carmichael et al. (2021). NGTS-19b is indicated in red.

brown dwarf and hot Jupiter systems (Rasio et al. 1996). We can apply this theory to NGTS-19b, to evaluate whether we would expect the orbit to have circularized, given the period and masses of the system. The majority of this orbital circularization is expected to occur early in the lifetime of the system, therefore if we determine a short orbital circularization time-scale for NGTS-19b it could be an indicator that the system is indeed young as suggested in Section 4.1.1.

We follow the method of Carmichael et al. (2020), based on the theoretical framework of Jackson, Greenberg & Barnes (2008). Here, the orbital circularization time-scales for the host star and brown dwarf are defined as

$$\frac{1}{\tau_{\text{circ},*}} = \frac{171}{16} \sqrt{\frac{G}{M_*}} \frac{R_*^5 M_{\text{BD}}}{Q_*} a^{-\frac{13}{2}}, \quad \text{and} \quad (1)$$

$$\frac{1}{\tau_{\text{circ,BD}}} = \frac{63}{4} \sqrt{\frac{GM_*^3}{Q_{\text{BD}} M_{\text{BD}}}} a^{-\frac{13}{2}}, \quad (2)$$

Table 6. Tidal circularization time-scale for NGTS-19b based on the tidal circularization model of Jackson et al. (2008), for a combination of reasonable stellar and brown dwarf tidal quality factors. For no realistic combination of tidal quality factors do we find a circularization time-scale that is reasonable.

Q_*	Q_{BD}	τ_e (Gyr)
10^5	$10^{4.5}$	18.39
10^6	$10^{4.5}$	169.10
10^7	$10^{4.5}$	934.54
10^5	10^5	18.52
10^6	10^5	180.18
10^5	10^6	18.58
10^6	10^6	185.23
10^7	10^6	1801.78

where a is the semimajor axis of the system, and Q_* and Q_{BD} are the tidal quality factors for the star and brown dwarf, respectively. From this, the circularization time-scale of the system is defined as

$$\frac{1}{\tau_e} = \frac{1}{\tau_{\text{circ},*}} + \frac{1}{\tau_{\text{circ},\text{BD}}} \quad (3)$$

From this, we can determine the circularization time-scale for the system. We note that this is typically applied to systems with lower eccentricities and shorter orbital periods than NGTS-19b. However, it is still a useful method for estimating whether or not we would expect a system of this type to have circularized in its lifetime. The tidal quality factors are rather poorly constrained in the literature, so as in Carmichael et al. (2020) we adopt a lower bound on Q_{BD} of $10^{4.5}$ based on the work of Beatty et al. (2018) on CWW 89Ab. We place a lower bound of 10^5 on Q_* based on previous studies of binary stars (Meibom & Mathieu 2005; Milliman et al. 2014).

In Table 6, we show the circularization time-scale for various combinations of both stellar and brown dwarf tidal quality factors. We find that there is no combination of tidal quality factors that provide a circularization time-scale of less than 18 Gyr, given the lower bounds we have placed. In fact, almost all combinations give a large circularization time-scale. Unless the tidal quality factors are substantially smaller than our lowest estimates (by at least an order of magnitude), we conclude that we would not expect the system to have been tidally circularized, and thus finding a brown dwarf of this orbital period and eccentricity is not unusual.

4.3 Future observing prospects

4.3.1 Secondary eclipse of NGTS-19b

It would be particularly valuable to our understanding on NGTS-19b if we were able to detect a secondary eclipse of the brown dwarf. Doing so would allow for direct determination of the brown dwarf temperature (as shown in Jackman et al. 2019). However, due to the significant difference in luminosity between the host star and the fainter brown dwarf, making such a detection is difficult.

For an eccentricity of $0.3767^{+0.0061}_{-0.0061}$ (assuming the argument of periastron in Table 5), we would expect to see a secondary eclipse at around phase $0.7075^{+0.0055}_{-0.0055}$. Both NGTS and *TESS* observations have coverage at this phase, so we examined their light curves for evidence of this secondary eclipse (Fig. 9). Despite the level of scatter in both

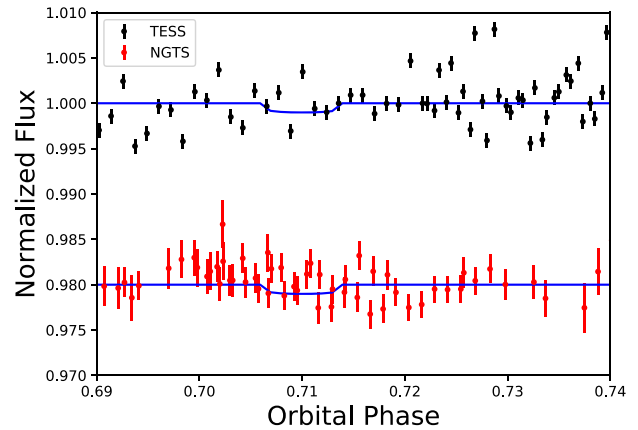


Figure 9. NGTS and *TESS* photometry for NGTS-19 around the expected phase of the secondary eclipse of the system. The NGTS data are binned to 30 min for comparison with the *TESS* full-frame image data. Overplotted in blue is a model of the maximum depth secondary eclipse for comparison. No obvious secondary eclipse is seen in either of the light curves.

light curves being very small (<0.1 per cent) for an object this faint, there is no obvious sign of a secondary eclipse seen in either of the light curves. Indeed, we searched a large range of orbital phase to account for any error in our calculation of orbital eccentricity, and we see no evidence for a secondary eclipse at any point. We note that for some objects in eccentric orbits we do not see a secondary eclipse at all, due to the system configuration and inclination. However, this is not the case for NGTS-19b where we would expect to see a secondary if the object had a high enough surface brightness, based on our modelling.

Based on the atmospheric models of Baraffe et al. (2003), an isolated $0.07 M_{\odot}$ brown dwarf has an effective temperature of 1626 K at 10 Gyr. If the system is young as speculated in Section 4.1, then the temperature could instead be as high as 2335 K. This leads to predicted secondary eclipse depths of ≈ 0.008 per cent and ≈ 0.09 per cent, respectively. This is within the scatter of both the NGTS and *TESS* light curves, and suggests that a non-detection is not unexpected. Due to the faint nature of this system, the detection of such a shallow secondary eclipse would be extremely challenging, even if the system is younger and more luminous than we expect. Based on this lack of secondary eclipse detection, we can place a tentative upper limit of ~ 2800 K on the brown dwarf temperature. For a temperature greater than this, we would expect the secondary eclipse to be large enough that it would be visible in the light curves. This places a lower limit on the age from the Baraffe et al. (2003) models of 0.1 Gyr, so it is not sufficient to constrain, confirm, or refute the suggested youth of the system, i.e. even if the brown dwarf is as young as suggested by its radius, we still would not expect to detect a secondary eclipse.

4.3.2 Spin-orbit angle

Transiting brown dwarfs present an interesting avenue to help understand the distribution seen in spin-orbit angle seen for exoplanets and low-mass stars. By measuring the Rossiter-McLaughlin effect, it has been shown that hot Jupiters can show a wide range of spin-orbit angles, with some even showing retrograde orbits (Queloz et al. 2010). However, similar studies of this effect for low-mass stars has shown that these systems do tend to be aligned (Triaud et al. 2013). This is likely due to the fact that hot Jupiters arrive into their short-

period orbits via dynamical interactions that force them into highly eccentric orbits that then circularize – leading to misalignment.

Brown dwarfs bridge the gap between planets and stars, so measuring the spin–orbit angle of transiting brown dwarfs allows for insight into what may cause the misalignment seen in planetary systems. For this system in particular, detection of a misaligned orbit may be some indication that the large eccentricity may not be primordial, and has caused interactions with a third body via Lidov–Kozai cycles (Kozai 1962; Lidov 1962). This would provide valuable insight into how a system such as this has formed and evolved.

The semi-amplitude of the Rossiter–McLaughlin effect scales approximately with planet size and stellar rotational velocity, in the following relation (Triaud 2018):

$$A_{\text{RM}} \approx \frac{2}{3} D v \sin(i) \sqrt{1 - b^2}, \quad (4)$$

where D is the transit depth ($\frac{R_{\text{BD}}}{R_*}$)², $v \sin(i)$ is the projected stellar rotation velocity, and b is the impact parameter. From analysis of the CORALIE spectra, we calculate $v \sin(i) = 2.1 \pm 0.4 \text{ km s}^{-1}$ for NGTS-19. This implies a Rossiter–McLaughlin amplitude of $13.4^{+2.7}_{-2.6} \text{ m s}^{-1}$. A signal of this magnitude could be detected easily with an instrument such as ESPRESSO (Pepe et al. 2021).

5 CONCLUSIONS

We report the discovery of a high-mass brown dwarf companion on a $P = 17.839654^{+0.000037}_{-0.000038}$ -d eccentric orbit around a main-sequence K-type star. NGTS-19b is a brown dwarf with a mass of $69.5^{+5.7}_{-5.4}$, placing it at the high end of the brown dwarf mass distribution. When compared to evolutionary models, the system is consistent with having an age of around 0.5 Gyr, although this is not consistent with age measurements from our spectroscopic or SED analysis, suggesting that the brown dwarf may be inflated due to interactions with its host star.

The system also has a highly eccentric orbit, with only two transiting brown dwarf systems being more eccentric. There are no shorter period, more eccentric transiting brown dwarfs known. When examined using established tidal circularization theory, we find that the system has a long enough period that we would not expect it to have been circularized in any reasonable time period.

NGTS-19b is the 29th transiting brown dwarf to be discovered, adding to the population of companions to main-sequence stars known as the brown dwarf desert. With the continuing survey of the *TESS*, mission it is quite possible that there will be many more additions to this once sparse region of parameter space in the years to come.

ACKNOWLEDGEMENTS

Based on data collected under the NGTS project at the ESO La Silla Paranal Observatory. The NGTS facility is operated by the consortium institutes with support from the UK Science and Technology Facilities Council (STFC) under projects ST/M001962/1 and ST/S002642/1. This paper includes data collected by the *TESS* mission. Funding for the *TESS* mission is provided by the NASA Explorer Program. This paper uses observations made at the South African Astronomical Observatory (SAAO).

JA is supported by an STFC studentship. This work has been carried out within the framework of the National Centre of Competence in Research Planets supported by the Swiss National Science Foundation. JSJ acknowledges support by FONDECYT grant 1201371, and partial support from CONICYT project Basal AFB-170002. MNG

acknowledges support from MIT’s Kavli Institute as a Juan Carlos Torres Fellow. EG gratefully acknowledges support from the David and Claudia Harding Foundation in the form of a Winton Exoplanet Fellowship.

DATA AVAILABILITY

The data underlying this article will be shared on reasonable request to the corresponding author.

REFERENCES

- Allard F., Homeier D., Freytag B., 2012, *Phil. Trans. R. Soc. A*, 370, 2765
 Baraffe I., Chabrier G., Allard F., Hauschildt P. H., 2002, *A&A*, 382, 563
 Baraffe I., Chabrier G., Barman T. S., Allard F., Hauschildt P. H., 2003, *A&A*, 402, 701
 Barbary K., 2016, *J. Open Source Softw.*, 1, 58
 Bayliss D. et al., 2017, *AJ*, 153, 15
 Beatty T. G., Morley C. V., Curtis J. L., Burrows A., Davenport J. R. A., Montet B. T., 2018, *AJ*, 156, 168
 Blanco-Cuaremas S., Soubiran C., Heiter U., Jofré P., 2014, *A&A*, 569, A111
 Borucki W. J. et al., 2010, *Science*, 327, 977
 Bouchy F. et al., 2011, *A&A*, 525, A68
 Burrows A., Heng K., Nampaisarn T., 2011, *ApJ*, 736, 47
 Carmichael T. W., Latham D. W., Vanderburg A. M., 2019, *AJ*, 158, 38
 Carmichael T. W. et al., 2020, *AJ*, 160, 53
 Carmichael T. W. et al., 2021, *AJ*, 161, 97
 Casewell S. L., Debes J., Braker I. P., Cushing M. C., Mace G., Marley M. S., Kirkpatrick J. D., 2020, *MNRAS*, 499, 5318
 Castelli F., Kurucz R. L., 2004, in Piskunov N., Weiss W. W., Gray D. F., eds, Proc. IAU Symp. 210, Modelling of Stellar Atmospheres. Kluwer, Dordrecht, p. A20
 Chaushev A. et al., 2019, *MNRAS*, 488, 5232
 Choi J., Dotter A., Conroy C., Cantiello M., Paxton B., Johnson B. D., 2016, *ApJ*, 823, 102
 Coppejans R. et al., 2013, *PASP*, 125, 976
 Csizmadia S. et al., 2015, *A&A*, 584, A13
 Cumming A., Butler R. P., Marcy G. W., Vogt S. S., Wright J. T., Fischer D. A., 2008, *PASP*, 120, 531
 David T. J., Hillenbrand L. A., Gillen E., Cody A. M., Howell S. B., Isaacson H. T., Livingston J. H., 2019, *ApJ*, 872, 161
 Folkes S. L. et al., 2012, *MNRAS*, 427, 3280
 Foreman-Mackey D., Hogg D. W., Lang D., Goodman J., 2013, *PASP*, 125, 306
 Gaia Collaboration, 2018, *A&A*, 616, A1
 Gill S. et al., 2020, *ApJ*, 898, L11
 Gillen E., Hillenbrand L. A., David T. J., Aigrain S., Rebull L., Stauffer J., Cody A. M., Queloz D., 2017, *ApJ*, 849, 11
 Gillen E., Hillenbrand L. A., Stauffer J., Aigrain S., Rebull L., Cody A. M., 2020, *MNRAS*, 495, 1531
 Grether D., Lineweaver C. H., 2006, *ApJ*, 640, 1051
 Günther M. N., Daylan T., 2019, Astrophysics Source Code Library, record ascl:1903.003
 Günther M. N., Daylan T., 2021, *ApJS*, 254, 13
 Hauschildt P. H., Allard F., Baron E., 1999, *ApJ*, 512, 377
 Husser T.-O., Wende-von Berg S., Dreizler S., Homeier D., Reiners A., Barman T., Hauschildt P. H., 2013, *A&A*, 553, A6
 Jackman J. A. G. et al., 2019, *MNRAS*, 489, 5146
 Jackson B., Greenberg R., Barnes R., 2008, *ApJ*, 678, 1396
 Jenkins J. S. et al., 2015, *MNRAS*, 453, 1439
 Kipping D. M., 2013, *MNRAS*, 435, 2152
 Kovács G., Zucker S., Mazeh T., 2016, Astrophysics Source Code Library, record ascl:1607.008
 Kozai Y., 1962, *AJ*, 67, 591
 Kurucz R. L., 1993, *VizieR Online Data Catalog*, Vol. 6039. Available at: <https://ui.adsabs.harvard.edu/abs/1993yCat.6039....0K/abstract>
 Lidov M. L., 1962, *Planet. Space Sci.*, 9, 719

- Marcy G. W., Butler R. P., 2000, *PASP*, 112, 137
- Marley M., Saumon D., Morley C., Fortney J., 2018, *Sonora 2018: Cloud-Free, Solar Composition, Solar C/O Substellar Atmosphere Models and Spectra*. Available at: <https://zenodo.org/record/1309035#.YMCJW34pDIV>
- Maxted P. F. L., 2016, *A&A*, 591, A111
- Meibom S., Mathieu R. D., 2005, *ApJ*, 620, 970
- Meisner A. M. et al., 2020, *ApJ*, 899, 123
- Méndez A., Rivera-Valentín E. G., 2017, *ApJ*, 837, L1
- Millholland S., Petigura E., Batygin K., 2020, *ApJ*, 897, 7
- Milliman K. E., Mathieu R. D., Geller A. M., Gosnell N. M., Meibom S., Platais I., 2014, *AJ*, 148, 38
- Moutou C. et al., 2013, *A&A*, 558, L6
- Nakajima T., Oppenheimer B. R., Kulkarni S. R., Golimowski D. A., Matthews K., Durrance S. T., 1995, *Nature*, 378, 463
- Nielsen E. L. et al., 2019, *AJ*, 158, 13
- Nowak G. et al., 2017, *AJ*, 153, 131
- Palle E. et al., 2021, preprint ([arXiv:2103.11150](https://arxiv.org/abs/2103.11150))
- Parsons S. G. et al., 2018, *MNRAS*, 481, 1083
- Parviainen H., Aigrain S., 2015, *MNRAS*, 453, 3821
- Pearson S., Scholz A., Teixeira P. S., Mužić K., Eislöffel J., 2020, *MNRAS*, 499, 2292
- Pecaut M. J., Mamajek E. E., 2013, *ApJS*, 208, 9
- Pepe F. et al., 2021, *A&A*, 645, A96
- Phillips M. W. et al., 2020, *A&A*, 637, A38
- Pinfield D. J. et al., 2008, *MNRAS*, 390, 304
- Queloz D. et al., 2000, *A&A*, 354, 99
- Queloz D. et al., 2010, *A&A*, 517, L1
- Rasio F. A., Tout C. A., Lubow S. H., Livio M., 1996, *ApJ*, 470, 1187
- Rebolo R., Zapatero Osorio M. R., Martín E. L., 1995, *Nature*, 377, 129
- Reylé C., 2018, *A&A*, 619, L8
- Ricker G. R. et al., 2015, *J. Astron. Telesc. Instrum. Syst.*, 1, 014003
- Rickman E. L. et al., 2019, *A&A*, 625, A71
- Saumon D., Marley M. S., 2008, *ApJ*, 689, 1327
- Schlafly E. F., Finkbeiner D. P., 2011, *ApJ*, 737, 103
- Schlegel D. J., Finkbeiner D. P., Davis M., 1998, *ApJ*, 500, 525
- Schneider A. C. et al., 2020, *ApJ*, 898, 77
- Sestovic M., Demory B.-O., Queloz D., 2018, *A&A*, 616, A76
- Siverv R. J. et al., 2012, *ApJ*, 761, 123
- Skrutskie M. F. et al., 2006, *AJ*, 131, 1163
- Spiegel D. S., Burrows A., Milsom J. A., 2011, *ApJ*, 727, 57
- Stassun K. G., Mathieu R. D., Valenti J. A., 2006, *Nature*, 440, 311
- Stassun K. G. et al., 2019, *AJ*, 158, 138
- Stelzer B., Marino A., Micela G., López-Santiago J., Liefke C., 2013, *MNRAS*, 431, 2063
- Tamaz O., Mazeh T., Zucker S., 2005, *MNRAS*, 356, 1466
- Triaud A. H. M. J., 2018, *Handbook of Exoplanets, The Rossiter-McLaughlin Effect in Exoplanet Research*. Springer International Publishing AG, New York, p. 2
- Triaud A. H. M. J. et al., 2013, *A&A*, 549, A18
- Triaud A. H. M. J. et al., 2017, *A&A*, 608, A129
- Vigan A. et al., 2020, preprint ([arXiv:2007.06573](https://arxiv.org/abs/2007.06573))
- Wheatley P. J. et al., 2018, *MNRAS*, 475, 4476
- Wright E. L. et al., 2010, *AJ*, 140, 1868
- Yee S. W., Petigura E. A., von Braun K., 2017, *ApJ*, 836, 77
- Zahn J. P., Bouchet L., 1989, *A&A*, 223, 112
- Zhou G. et al., 2019, *AJ*, 157, 31

This paper has been typeset from a $\text{\TeX}/\text{\LaTeX}$ file prepared by the author.